



Ionization-Gasdynamics Models and X-ray Spectra of Wind-Blown Nebulae around Massive Stars

V. V. Dwarkadas^a, D. L. Rosenberg^b

^a*Department of Astronomy and astrophysics, Univ of Chicago, TAAC 55, Chicago, IL 60637*

^b*National Center for Atmospheric Research, Boulder, Colorado*

Abstract

We describe an ionization gasdynamics code to study astrophysical systems where the gas-dynamics must be computed in tandem with the photo-ionization from a source. We use it to compute a model of the wind-blown bubble around a $40 M_{\odot}$ star, and from this, to accurately compute the X-ray emission from the bubble. We outline our methods and techniques for these computations, compare them with previous calculations, and show how they relate to observations. Our simulated X-ray spectra suggest that X-ray nebulae around massive stars may not be easily detectable, consistent with observations.

© 2011 Published by Elsevier Ltd.

Keywords:

Stars: massive, Stars: mass-loss, Stars: winds, outflows, ISM: bubbles, circumstellar matter, X-rays: ISM

1. Introduction

Massive stars ($> 8M_{\odot}$) lose mass throughout their lifetime, via winds and eruptions, before ending their lives in a cataclysmic supernova (SN) explosion. The interaction of this material with the surrounding medium creates vast wind-blown cavities surrounded by a dense shell, referred to as wind-blown bubbles. Simultaneously, radiation from the star can ionize the surrounding medium. As the star evolves through various stages, the mass-loss parameters, and the ionizing flux or number of ionizing photons, will change, affecting the structure of the bubble. When the star finally explodes, the resulting SN shock wave will expand within the bubble, and the dynamics and kinematics of the shock wave will depend on the bubble parameters [8]. Similarly, the relativistic blast waves associated with gamma-ray bursts (GRBs) are expected to expand within wind bubbles surrounding Wolf-Rayet (W-R) stars. Thus, it is important to understand the structure of the bubble, as it influences the evolution and emission from SNe and GRBs.

The structure of wind bubbles was identified by Weaver et al. [26]. Proceeding radially outward from the star, 4 regions are delineated: (1) a freely expanding wind region, (2) a shocked wind region, (3) the shocked ambient region, forming a thin dense shell, and (4) the unshocked ambient medium. An inner, ‘wind termination’ shock separates region (1) and (2), a contact discontinuity, regions (2) and (3) and an outer, generally radiative shock, regions (3) and (4).

In order to understand the structure of wind-bubbles accurately, models must take into account both the gasdynamics and ionization from the star. Early models that explored the evolution of massive star surroundings [16, 17]

Email addresses: vikram@oddjob.uchicago.edu (V. V. Dwarkadas), duaner@ucar.edu (D. L. Rosenberg)

had some ionization built in, mainly centered around the Stromgren sphere approximation. They did not model the main-sequence (MS) stage in multi-dimensions. Similar limitations were included in the models of [25, 24]. A somewhat better treatment of ionization properties was included in [14, 15]. Dwarkadas [9, 10, 11] considered the entire evolution in multi-dimensions, and studied the turbulence in the interior, but did not include any ionization in his calculations. 3D simulations carried out by [23] also do not include ionization. A more complete treatment of both the ionization plus the gasdynamics has been included in the work of Arthur and her group [2, 3, 22].

In this paper we describe a new code that couples the ionization to the gasdynamics, and use it to study the evolution of wind bubbles around a $40 M_{\odot}$ star. Using our code, AVATAR, we compute the structure and evolution of the wind-blown bubble, study the dynamics, hydrodynamics and kinematics, the formation of instabilities, growth of small scale structure, and the onset of turbulence.

Much of the volume of the wind bubble is occupied by the high-pressure, low density shocked wind. Wind velocities of order $1000\text{--}2000 \text{ km s}^{-1}$ for O, B and Wolf-Rayet (W-R) stars should conceivably result in post-shock temperatures in the shocked wind of $10^7 - 10^8 \text{ K}$. It has been assumed in the literature, perhaps rather naively, that the nebulae should therefore be visible as regions of diffuse X-ray emission. However, despite extensive searches around WR and main-sequence stars with Chandra and XMM, diffuse X-ray emission has been detected in only few cases [5, 4, 28], with observed X-ray luminosities 10-100 times smaller than would be expected given the “expected” temperatures and the size of the region. The inferred temperatures for bubbles around two W-R stars, NGC 6888 and S308, are a few times 10^6 K , again lower than expected given the wind velocities. Recently, Zhekov & Park [29] have found that about 10% of the flux in 6888 arises from higher temperature plasma ($> 2 \text{ keV}$).

It appears that either some of the a-priori assumptions must be incorrect, or perhaps that the thermal energy is converted to some other form of energy. Turbulence has been suggested as one answer. Dwarkadas [11] found, from 2D simulations, that only a small percentage of the energy went into turbulent motions, except in the very last stages of W-R evolution, where the energy in non-radial motions was about 15-20% of that in the radial flow. Thermal conduction is another suggestion, but given the low densities within the bubble, it seems quite unlikely. This has been quantitatively shown by [22]. In order to address questions regarding the X-ray emission, we compute X-ray spectra from our simulations, using the ISIS package [18].

This paper proceeds as follows: In §2 we describe the photoionization code, and in §3 the numerical methods. These are then applied to modelling the medium around a $40 M_{\odot}$ star in §4, and X-ray spectra computed from the models in §5. §6 summarizes our work and outlines future development.

2. PhotoIonization Code

To simplify the calculations and the problem description, it is assumed that hydrogen is the only component of the gas that undergoes photoionization and recombination. The full radiation gasdynamic equations that are solved are the usual equations describing mass, momentum and energy conservation:

$$\partial_t \rho_H + \nabla \cdot (\rho_H \mathbf{v}) = 0 \quad (1)$$

$$\partial_t \rho_{HI} + \nabla \cdot (\rho_{HI} \mathbf{v}) = \rho_H [x n_e \alpha_R(T) - (1-x) \phi_{\text{phot}} - (1-x) n_e A_{\text{coll}}(T)] \quad (2)$$

$$\partial_t \mathbf{s}_i + \nabla \cdot (s_i \mathbf{v}) + \nabla p = 0 \quad (3)$$

$$\partial_t e + \nabla \cdot (e \mathbf{v}) + p \nabla \cdot \mathbf{v} = n_{HI} \Gamma_{\text{phot}} - f(x, T) n_H^2 \Lambda(T) \quad (4)$$

where ρ_H is the total (neutral and ionized) mass density, ρ_{HI} is the neutral hydrogen density, e is the internal energy (see below), p is the isotropic pressure, \mathbf{v} is the local fluid velocity and, and s_i represents the r - and θ -components of momentum. A separate transport equation (equation (2)) is provided for the neutral hydrogen density. This additional equation is required in the event that the characteristic transport time is shorter than the local photoionization or heating/cooling time. In principle, separate transport equations would also be included for ionization states of other elements. The right hand sides of equations (2) and (4) contain the source terms for photoionization and heating, respectively, which are of interest here.

In these equations x is the ionization fraction, ϕ_{phot} represents the number of ionizing photons per second from the central star, A_{coll} is the coefficient for collisional ionization in $\text{cm}^3 \text{ s}^{-1}$, Γ_{phot} is the heating rate per neutral hydrogen atom due to the star in erg s^{-1} , Λ is the cooling function in $\text{erg cm}^3 \text{ s}^{-1}$, and $\alpha_R = 2.59 \times 10^{-13} \text{ cm}^3 \text{ s}^{-1} (T/10^4 \text{ K})^{-0.8}$ is

the hydrogen recombination coefficient [19, 13]. The total number density is $n = n_e + n_H$, where $n_e = n_p = xn_H$ is the electron (proton) number density, $n_H = n_p + n_{HI}$ is the hydrogen number density, and $n_{HI} = (1 - x)n_H$ is the neutral hydrogen density. The hydrogen number density is obtained from the mass density, $n_H = \rho_H/m_p$ (m_p is the proton mass), and the temperature is computed from equations (5) and (6) (see below).

The internal energy, e , is defined as

$$e = \frac{p}{\gamma - 1} + xn_H I_H, \quad (5)$$

where I_H is the ionization potential for hydrogen, and $\gamma = 5/3$ is the adiabatic index. A single temperature, T , is assumed for the neutral and ionized components and for the electrons in a cell. Thus, the first term of the internal energy, due solely to translational degrees of freedom, can be given in terms of T since

$$p = (1 + x)n_H kT, \quad (6)$$

where k is the Boltzmann constant.

Tabulated functions are used in computing the collisional ionization rate and the cooling function. In computing the cooling rate, an approximation to a full non-equilibrium treatment is used. If $T \gtrsim 10^4 \text{K}$, the gas is essentially completely ionized, in which case, the curve taken from Fig. 2 of [6] is adequate, and $f(x, T) = 1$. For $T \lesssim 10^4$, the $x = 0.1$ curve of [6] is used, scaled by $f(x, T) = x/0.1$ when $x \leq 0.1$. In order to model higher ionization states than those allowed by the [6] curve when $T \lesssim 10^4$, such as those encountered in HII regions, $\Lambda(T)$ is taken from Fig. 3.2 of [19] when $x > 0.1$, where $f(x, T) = 1$.

To calculate ϕ_{phot} and Γ_{phot} , the method of [13] is used, although only hydrogen absorption is treated. However, the numerical method can be easily adapted to accommodate ionization states of other elements (see §3). The photon number flux and the photoionization heating rate are defined from the following flux integrals:

$$\phi_{\text{phot}} = \int_{\nu_0}^{\infty} \frac{4\pi J_\nu}{h\nu} a_{\nu,H} d\nu, \quad (7)$$

and

$$\Gamma_{\text{phot}} = \int_{\nu_0}^{\infty} \frac{4\pi J_\nu}{h\nu} a_{\nu,H} h(\nu - \nu_0) d\nu, \quad (8)$$

where ν_0 is the ionization threshold for hydrogen (Lyman limit), $a_{\nu,H}$, the photoionization cross section, and J_ν is the mean intensity of radiation. Using the ‘‘on the spot’’ approximation and considering only the radial transport of radiation, the intensity can be written

$$J_\nu = \left(\frac{R_*}{r}\right)^2 F_\nu e^{-\tau_\nu(r)}, \quad (9)$$

where $\tau_\nu(r) \approx \tau_{\nu_0} a_\nu / a_{\nu_0}$ is the optical depth at r [19]. The optical depth at the threshold is obtained by integrating in r : for zone i , it is $\tau_{\nu_0,i} = \tau_{\nu_0,i-1} + n_H a_\nu \Delta r$. F_ν is the stellar spectrum at the photospheric radius, R_* . In principle, any model spectrum could be chosen, but for simplicity, a blackbody spectrum is used ($F_\nu = B_\nu$). Γ_{phot} is defined slightly differently than in [13], in order to make the dependence on x and n explicit. The flux integrals are calculated initially as a function of τ_{ν_0} and stored in look-up tables. These tabulated integrals are then interpolated using the optical depth of the zone whose solution is being sought. These integrals can be computed on each timestep in order to model an evolving photoionizing source, but that is computationally expensive.

3. Numerical Method

The numerical computations must solve Eqs. (1)-(4) describing the gasdynamics and the photoionization and heating processes. The gasdynamic algorithm makes use of a multidimensional covariant implementation of well established Eulerian finite difference algorithms [20]. A second-order (van Leer) monotonic transport algorithm is used for the advection of total mass and the neutral component. Shocks are treated using an artificial viscosity. Grid expansion may be required in order to study the flow over distance scales spanning several orders of magnitude; it may be critical in certain applications. Reference is made to a spherical-polar (r - θ) coordinate system in this discussion, but it is clear that the method is independent of the choice of coordinate system, and dimensionality.

By operator splitting the photoionization source terms may be separated from the above equations:

$$\frac{\partial x}{\partial t} = (1-x)\phi_{\text{phot}} + (1-x)n_e A_{\text{coll}}(T) - xn_e \alpha_R(T) \quad (10)$$

$$\frac{\partial e}{\partial t} = n_H I \Gamma_{\text{phot}} - f(x, T) n_H^2 \Lambda(T), \quad (11)$$

where the ionization fraction is solved for explicitly, instead of the neutral density. These equations take the general vector form

$$\partial_t \mathbf{y} = \mathbf{R}(\mathbf{y}) \quad (12)$$

where $\mathbf{y} = (x, e)$ and $\mathbf{R}(\mathbf{y})$ is the vector of the right hand side source terms. The finite difference approximation to Eq. (12) becomes

$$\tilde{\mathbf{y}} - \mathbf{y}^n = \Delta t \mathbf{R}(\mathbf{y})$$

where $\tilde{\mathbf{y}}$ is the solution sought, \mathbf{y}^n is the most recent (converged) time-updated value of \mathbf{y} , \mathbf{R} is evaluated at the new \mathbf{y} , and Δt is the hydrodynamic Courant limited timestep. This implicit difference expression is the backward Euler scheme. Thus the roots of the equation

$$\Gamma(\mathbf{y}) = \mathbf{y} - \mathbf{y}^n - \Delta t \mathbf{R}(\mathbf{y}) = 0 \quad (13)$$

are required. This is a highly nonlinear equation, whose solution can be determined iteratively by linearizing:

$$\Gamma(\mathbf{y}' + \delta \mathbf{y}') = \Gamma(\mathbf{y}') + (\mathbf{1} - \Delta t \frac{\partial \mathbf{R}}{\partial \mathbf{y}}) \delta \mathbf{y}' = 0.$$

This is the Newton-Raphson scheme to find the corrections, $\delta \mathbf{y}'$, that iterate \mathbf{y}' closer to the solution of Eq. (13). The quantity $\partial \mathbf{R} / \partial \mathbf{y}$ is the Jacobian rate matrix evaluated at the most recent iterate, \mathbf{y}' . Solving for $\delta \mathbf{y}'$:

$$\delta \mathbf{y}' = (\mathbf{1} - \Delta t \frac{\partial \mathbf{R}}{\partial \mathbf{y}})^{-1} [\mathbf{y}^n - \mathbf{y}' + \Delta t \mathbf{R}(\mathbf{y}')] \quad (14)$$

Note that the flux integrals, Eqs. (7)-(8)), require that the equations be integrated in radius. The algorithm may not proceed to a subsequent radial zone until a solution has been achieved at all angular zones in the previous radial zone. Thus, the solution is naturally vectorizable, with the vectors representing angular slices at a constant radial index. The solution is computed in two steps: in the first, a solution is attempted at the hydro timestep; in the second, subcycling is carried out over this timestep to integrate the solution for those zones that did not converge at the hydro timestep.

To begin the iterative process, the algorithm starts at the initial radius, sets $\mathbf{y}' = \mathbf{y}^n = \mathbf{y}_h$, where \mathbf{y}_h is the value derived from the gasdynamics partial update, and sets Δt to the hydro timestep. The rate matrix and \mathbf{R} are computed at this value of \mathbf{y}' , and $\delta \mathbf{y}'$ is computed from Eq. (14). With this correction, the solution can be updated via $\mathbf{y}' \rightarrow \mathbf{y}' + \delta \mathbf{y}'$ for the next iteration. This iterative procedure is continued until all angular zones converge, such that $\delta \mathbf{y}' / \mathbf{y}' < \epsilon_{\text{NR}}$, where typically, $\epsilon_{\text{NR}} = 10^{-3}$. If any zone fails to meet the condition $\delta \mathbf{y}' / \mathbf{y}' < \epsilon_{\text{min}} \sim 0.3$, it is not iterated upon further. This additional condition is introduced in order to speed convergence. The iteration procedure is completed if either all zones have converged or if there are no zones left to iterate upon. The converged zones are called partially converged, and the best estimate for the solution at the hydro timestep is taken to be $\tilde{\mathbf{y}} = \mathbf{y}'$.

Next, a check is made to determine if the partially converged zones meet a time stability requirement. A zone is said to be fully converged if $|\tilde{\mathbf{y}} - \mathbf{y}^n| / \mathbf{y}_h < \epsilon_1$, where $\epsilon_1 \sim 0.2$. If any zones fail to meet the partial or full convergence criteria, Δt is reduced, and the failed zones are subcycled at the reduced timestep using the above procedure, with the following changes: as the solution becomes fully converged at the reduced timestep, the condition $\mathbf{y}^n = \tilde{\mathbf{y}}$ is set for the next subcycle, and the subcycling timestep is adjusted so that it does not exceed the hydro timestep.

In many (particularly two dimensional) cases anomalously high cooling rates have been observed at contact discontinuities and shocks where these features are spread out over several zones. To correct this problem, the procedure used by [21] is applied: if a given zone, i , has a cooling rate greater than $f \sim 2$ times that of both of its nearest neighbors in the r or θ directions, then the average per-unit-volume cooling rate of the neighboring zones is used for cooling rate in the zone. Since the rate equations are integrated radially, the cooling at (r_{i+1}) can not be computed until convergence is achieved at r_i . An estimate of the cooling rate must then be made. To do this, Λ is assumed to be

constant at the level of the current iterate in the i^{th} zone, and the density change alone is used to compute the cooling rate at r_{i+1} . It is noted that another way of reducing the effects of this anomaly is to use a higher order advection scheme, such as PPM, in order to more accurately localize sharp features.

By considering the linearization it becomes clear how the method may be augmented, in principle, to include ionization states of additional atomic species other than hydrogen. There exists for each species a rate equation that governs the detailed balance of loss (through ionization) and gain (through recombination to various energy levels). Additionally the heating term must account for the contributions due to the ionization of the species. Cooling must also account for the additional ionic species; a non-equilibrium treatment may be required (e.g., [13]). With these additions, the rate matrix is expanded, but the algorithm operates in the same manner. The only other requirement is that the gasdynamic equations include the appropriate transport terms for the new ionic species.

4. Hydrodynamic Models

We apply the AVATAR code to the computation of the wind-blown bubble around a $40 M_{\odot}$ star. The simulations are carried out on an r - θ grid in spherical co-ordinates. Runs with varying resolution were computed, with the largest being 600 radial by 400 angular zones. The runs are carried out on a single processor, with the largest taking almost two weeks to run. The stellar parameters for the $40 M_{\odot}$ star are adapted from [25]. The star evolves from the MS stage into a red-supergiant (RSG), and finally ends its life as a W-R star before it explodes. Although realistically the stellar parameters are continuously changing, this would make it extremely time consuming to calculate the ionization integrals at every timestep. Therefore the stellar parameters in each phase are assumed constant, as suggested by [25]. In this way the integrals need to be computed only once per stage. In future we will modify this so that we can take the changing mass-loss rates into account, since these are important to study the turbulence and instabilities within the bubble.

Figure 1 shows the density, ionization and temperature of the star during the various stages. The star starts life as a main-sequence (MS) O star, and remains on the MS for about 4.3 million years, with a fast, radiatively-driven wind. In this phase almost the entire bubble is fully ionized (Fig. 1, row 2 column 1). An inhomogeneous pressure and density distribution develops in the MS stage, accompanied by vorticity deposition near the inner shock. The inclusion of photo-ionization results in the formation of a dense, lower temperature ($\sim 10^4$ K) region of ionized material (orange) outside the wind bubble during the MS phase. The nebula is fully ionized, and the ionization front is trapped in the dense shell. The ionization front is unstable to ionization-driven instabilities, reminiscent of Rayleigh-Taylor instabilities, which are also seen in galactic ionization fronts [27]. We also see finger-like projections protruding from the ionized region into the interior, which may be the forerunners of the photo-ionized pillars seen for instance in the Eagle Nebula, and studied in detail by Mackey (HEDP, submitted).

As the star moves off the MS into the red supergiant (RSG) stage, the mass-loss rate increases sharply to almost $10^{-4} M_{\odot} \text{yr}^{-1}$, and the wind velocity drops to about 15 km s^{-1} . Although much of the mass from the star is lost in this stage, the RSG wind fills only a small fraction of the bubble. The surface temperature being much lower, the star is no longer able to ionize the entire region. The ionizing radiation drops considerably and recombination reduces the ionization fraction to $\sim 30\%$ in the outer regions (Fig 1, row 2 column 2). As shown in [10], the RSG shell is also unstable. After about 200,000 years in the RSG stage, the star loses its outer envelope and becomes a W-R star, with a fast wind and a mass-loss rate only slightly lower than that in the RSG phase. The high temperature of the W-R star re-ionizes the entire region. The higher momentum W-R wind, due to its high velocity, collides with the dense RSG shell and breaks it up, scattering the dense material into a turbulent W-R nebula.

Turbulence within the bubble leads to the formation of vortices in the interior of the bubble in the MS stage, driven by deposition of vorticity at the reverse shock. This is accentuated by the 2D nature of the simulation, since 2D turbulence results in an inverse cascade in energy [11]. The turbulence decreases in the RSG phase. The collision of the W-R and RSG shells leads to an increase in turbulence in the final stages of the bubble, leading to a messy structure into which any subsequent supernova shock wave will expand.

The temperature of the nebula during the evolution is shown in the bottom row of Fig 1. Note how, in the early W-R stage, the temperature is still low in the outer wind-blown bubble. Thermal conduction has been suggested to reduce the temperature (e.g. Zhekov & Park 2011), but our calculations do not show any need for it.

How do our models compare to previous work? The gross features have been outlined in many of the works mentioned in §1, and our models as expected do faithfully reproduce them. Interestingly, our models reproduce

multi-dimensional features such as ionization front instabilities, seen in many galactic ionization front models [27] but not mentioned in previous simulations of wind bubbles. The closest work to which our models could be compared are those of [3, 22]. Our 1D models (not shown) agree quite well with their 1D simulations when run with similar parameters, although our resolution of tens of thousands of zones seems much higher. The 2D models shown here are harder to compare without having quantitative data. It is clear that we again reproduce the basic features. Our shock fronts seem sharper and instabilities far more pronounced, although it is not clear whether this is a resolution effect, or merely due to the reproduction of the figures in the papers from Arthur’s group. One thing that our simulations reveal clearly is the recombination of the material in the red-supergiant stage as the surface temperature of the star dramatically decreases, leading to a large decrease in the ionization fraction. This is visible in some of their 1D simulations, but there are no good figures clearly illustrating the evolution of the ionization fraction in their multi-dimensional models. We feel that, while all models reproduce the gross features, our work improves on previous work in terms of capturing the various discontinuities, elucidating the turbulence and instabilities, and understanding the evolution of the ionization fraction.

5. X-ray Emission:

Having computed the structure of the bubble, we proceed to compute the X-ray spectrum from the bubble at each timestep. We use the ISIS package [18] to compute the X-ray emission. The `vmekal` model in XSPEC, commonly used to fit the observed X-ray spectra [5], is used to model the spectrum, although any other available XSPEC model can be substituted. We have also tried the Raymond-Smith model (`vraymond`), with similar results.

The 2D data are read into ISIS, and the spectrum calculated in each cell given the values of the various quantities (temperature, density, velocity etc.) in that cell. For the run presented here that means computing the spectrum in 240,000 cells. The absorption column beyond that cell is calculated, summed over all cells along the radius, and used to calculate the absorption. The spectra presented herein (Fig 2) are convolved with the Chandra ACIS instrument response and area functions, for an object at 1.5kpc distance, integrated over 50,000 s. Foreground absorption of $2 \times 10^{20} \text{ cm}^{-2}$ is added to absorption by neutral material surrounding the bubble, which can be as high as $2 \times 10^{21} \text{ cm}^{-2}$ (total absorption column given on figure title is in units of 10^{22} cm^{-2}). Line broadening is added based on the underlying fluid velocity. Solar abundances [1] are used for the MS and RSG stages, while abundances in the W-R phase are from [5] for the W-R bubble S308, one of two W-R bubbles to be detected in diffuse X-rays.

Although no attempt has been made to fit to a specific bubble, the resulting X-ray spectra do show resemblance to observed X-ray spectra given in [5, 29]. The computed spectra are quite soft, generally peaking at or below 1 keV. In this they resemble those shown by [22], although our spectra show better energy resolution. The spectra in [22] appear to have somewhat similar shape at certain epochs, but much higher counts. Exact comparison is not possible because their spectra are convolved with the instrument response for EPIC/pn on *XMM-newton*, and the integration time is not given. The emission appears to arise primarily from the denser regions, including the instabilities and resulting dense clumps that are formed. The volume of the emitting region is reduced by the presence of the ionized region surrounding it, and the temperatures are found to be lower due to recombination in the RSG stage. Spectra are calculated in ionization equilibrium. While we have recently developed the capability to carry out non-equilibrium ionization calculations in the case of 1D calculations [12, 7], we are still in the process of expanding this capability to multi-dimensional calculations. However, such complexity does not seem to be required to reproduce the observed X-ray spectra, especially given that much of the material in the bubble is over 10^5 years old.

6. Summary

Using a new code that employs a self-consistent method for computing the effects of photo-ionization on circum-stellar gas dynamics, we have modeled the formation of wind-driven nebulae around massive stars. Our algorithm incorporates a simplified model of the photo-ionization source, computes the fractional ionization of hydrogen due to the photo-ionizing flux and recombination, and determines self-consistently the energy balance due to ionization, photo-heating and radiative cooling, taking into account the effects of geometrical dilution and of column absorption of radiation. Shocks are treated using an artificial viscosity, and grid expansion is available. We take into account changes in stellar properties and in stellar mass-loss over the star’s evolution. Our multi-dimensional simulations reveal the presence of strong ionization front instabilities, similar to those seen in galactic ionization fronts.

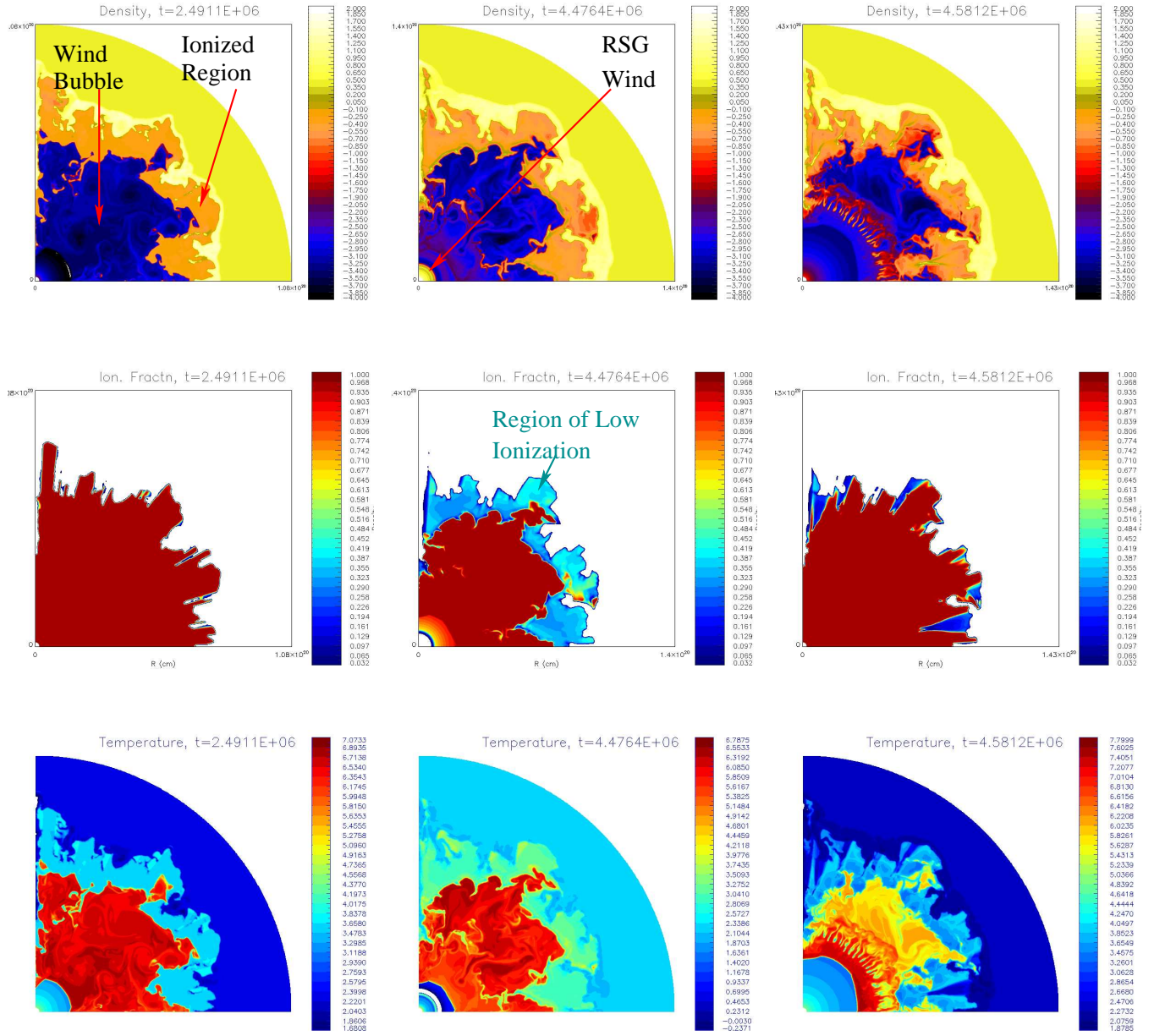


Figure 1. Snapshots from a calculation of a wind bubble evolution around a $40 M_{\odot}$ star (600×400 zones), computed with AVATAR using an expanding grid. Density (top row), ionization fraction (middle row), and temperature (bottom row). L \Rightarrow R (a) The MS wind bubble (dark blue), expanding within an ionized region (orange) formed by photo-ionization. The ionization front is trapped in the dense shell (thin light yellow region), which is unstable to ionization front instabilities. The wind bubble is hot, but the ionized region is only at $\sim 10^4$ K (b) The RSG shell within the MS bubble, a few parsecs from the star. In the RSG stage the star is cool, the ionization fraction decreases considerably, and the material in the bubble interior, starting at larger radii, begins to recombine. (c) The W-R wind, which breaks up the RSG shell, distributing its contents. Note the turbulent nature of the interior. The temperature slowly rises to X-ray producing levels again, but is still low in the outer parts.

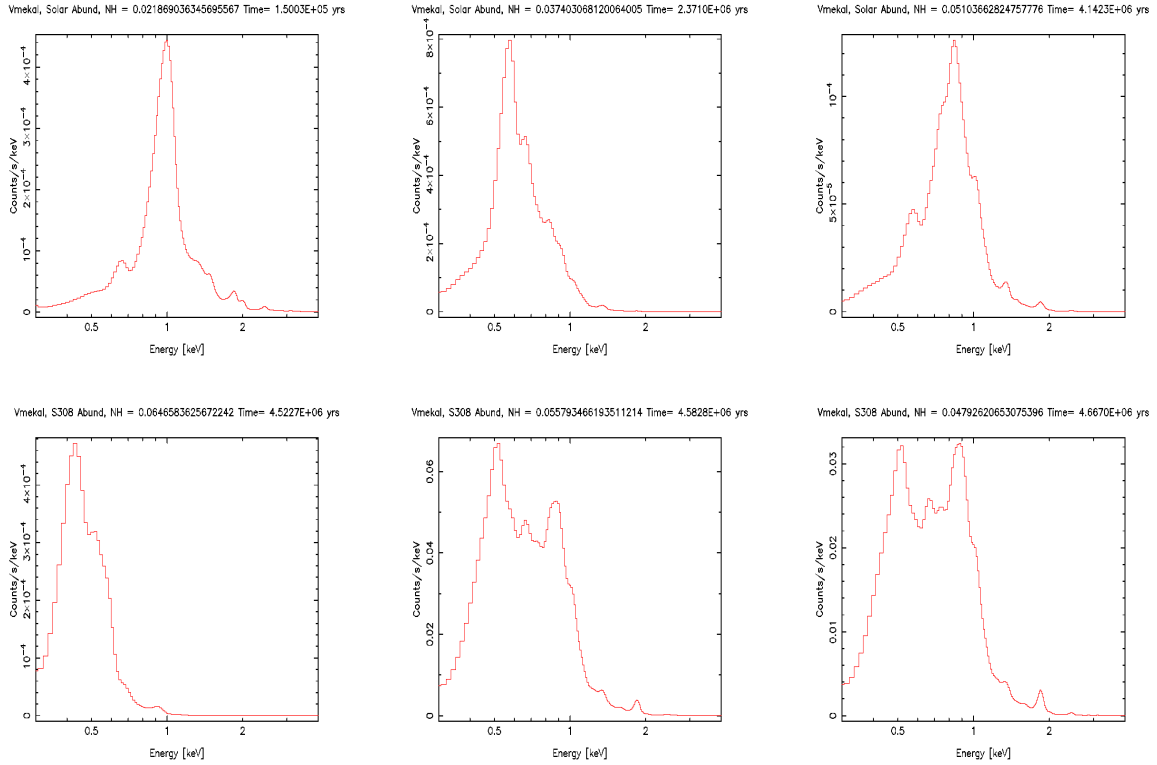


Figure 2. (LHS) Simulated X-ray spectra for a point source calculated from simulations shown in Fig 1. The spectra were calculated from a single simulation. The first 3 are computed when the nebula is in the MS stage, the next 3 in the W-R stage. Solar abundances were assumed for the MS stage, while abundances characteristic of S308 were used for the W-R stage. The X-ray model used, the absorption column (in units of 10^{22}cm^{-2}) and the Time in years is noted in the title of each plot. The scale is the count-rate that would be received for a source at 1.5 kpc distance in a 50 ks ACIS observation. The count rate is generally very low in our simulated spectra in the MS stage, about 10^{-4} counts $\text{s}^{-1} \text{keV}^{-1}$, and it is clear that such a bubble would not be visible in X-rays in the MS phase. It can rise by about 2 orders of magnitude or so towards the end of the W-R stage, which is still quite low as compared to the data on S308. This seems to be generally true over all our simulations, in agreement with the fact that diffuse X-ray emission is not generally observed.

Using various X-ray emission models, we have computed detailed X-ray spectra of simulated wind-blown nebulae from a $40 M_{\odot}$ star, as would be seen with the ACIS instrument on Chandra. Comparing with observed X-ray spectra, we find that at certain epochs of the evolution, our synthetic spectra in the Wolf-Rayet (W-R) stage agree quite well with those obtained from observed W-R nebulae. Unlike other calculations, our detailed spectra indicate that diffuse X-ray emission from most main sequence and W-R nebulae would *not* be easily observable with currently available X-ray satellites, which is consistent with the observational data [5, 4].

In future we will present calculations for the wind medium around stars of varying initial mass, taking stellar models with rotation and magnetic field into account. We will also compute the X-ray emission using different XSPEC models, study the locations from which the X-ray emission arises, and produce maps showing the cells that are major contributors to the X-ray emission. These can be compared to density and temperature maps to fully understand which regions are the major contributors to the X-ray emission, and why the spectra are so soft.

7. Acknowledgements

VVDs research was funded by grant TM9-0001X, provided by NASA through the Chandra X-ray Observatory center, operated by SAO under NASA contract NAS8-03060. DLR wishes to acknowledge sponsorship of this work

from an NSF cooperative agreement through the University Corporation for Atmospheric Research on behalf of the National Center for Atmospheric Research (NCAR). We are grateful to Dan Dewey for patiently answering our questions and being super helpful in general.

References

- [1] Anders, E. and Grevesse, N. [1989], ‘Abundances of the elements - Meteoritic and solar’, *GeCoA* **53**, 197–214.
- [2] Arthur, S. J. [2007], Wind-Blown Bubbles and HII Regions around Massive Stars, in ‘Revista Mexicana de Astronomia y Astrofisica Conference Series’, Vol. 30 of *Revista Mexicana de Astronomia y Astrofisica Conference Series*, pp. 64–71.
- [3] Arthur, S. J. [2009], Dynamics of Bubbles in the ISM, in R. K. Smith, S. L. Snowden and K. D. Kuntz, eds, ‘American Institute of Physics Conference Series’, Vol. 1156 of *American Institute of Physics Conference Series*, pp. 285–294.
- [4] Chu, Y.-H., Gruendl, R. A. and Guerrero, M. A. [2003], An Inside-Out View of Bubbles, in J. Arthur and W. J. Henney, eds, ‘Revista Mexicana de Astronomia y Astrofisica Conference Series’, Vol. 15 of *Revista Mexicana de Astronomia y Astrofisica*, vol. 27, pp. 62–67.
- [5] Chu, Y.-H., Guerrero, M. A., Gruendl, R. A., García-Segura, G. and Wendker, H. J. [2003], ‘Hot Gas in the Circumstellar Bubble S308’, *ApJ* **599**, 1189–1195.
- [6] Dalgarno, A. and McCray, R. A. [1972], ‘Heating and Ionization of HI Regions’, *ARAA* **10**, 375.
- [7] Dewey, D., Dwarkadas, V. V., Haberl, F., Sturm, R. and Canizares, C. R. [2012], ‘Evolution and Hydrodynamics of the Very Broad X-Ray Line Emission in SN1987A’, *ApJ* **752**, 103.
- [8] Dwarkadas, V. V. [2005], ‘The Evolution of Supernovae in Circumstellar Wind-Blown Bubbles. I. Introduction and One-Dimensional Calculations’, *ApJ* **630**, 892–910.
- [9] Dwarkadas, V. V. [2007a], ‘Hydrodynamics of Supernova Evolution in the Winds of Massive Stars’, *ApSS* **307**, 153–158.
- [10] Dwarkadas, V. V. [2007b], ‘The Evolution of Supernovae in Circumstellar Wind Bubbles. II. Case of a Wolf-Rayet Star’, *ApJ* **667**, 226–247.
- [11] Dwarkadas, V. V. [2008], ‘Turbulence in wind-blown bubbles around massive stars’, *Physica Scripta Volume T* **132**(1), 014024.
- [12] Dwarkadas, V. V., Dewey, D. and Bauer, F. [2010], ‘Bursting SN 1996cr’s bubble: hydrodynamic and X-ray modelling of its circumstellar medium’, *MNRAS* **407**, 812–829.
- [13] Frank, A. and Mellema, G. [1994], ‘A radiation-gasdynamical method for numerical simulations of ionized nebulae: Radiation-gasdynamics of PNe I’, *AA* **289**, 937–945.
- [14] Freyer, T., Hensler, G. and Yorke, H. W. [2003], ‘Massive Stars and the Energy Balance of the Interstellar Medium. I. The Impact of an Isolated 60 Msolar Star’, *ApJ* **594**, 888–910.
- [15] Freyer, T., Hensler, G. and Yorke, H. W. [2006], ‘Massive Stars and the Energy Balance of the Interstellar Medium. II. The 35 Msolar Star and a Solution to the “Missing Wind Problem”’, *ApJ* **638**, 262–280.
- [16] Garcia-Segura, G., Langer, N. and Mac Low, M.-M. [1996], ‘The hydrodynamic evolution of circumstellar gas around massive stars. II. The impact of the time sequence O star - RSG - WR star.’, *AA* **316**, 133–146.
- [17] Garcia-Segura, G., Mac Low, M.-M. and Langer, N. [1996], ‘The dynamical evolution of circumstellar gas around massive stars. I. The impact of the time sequence Ostar - LBV - WR star.’, *AA* **305**, 229.
- [18] Houck, J. C. and Denicola, L. A. [2000], ISIS: An Interactive Spectral Interpretation System for High Resolution X-Ray Spectroscopy, in N. Manset, C. Veillet, & D. Crabtree, ed., ‘Astronomical Data Analysis Software and Systems IX’, Vol. 216 of *Astronomical Society of the Pacific Conference Series*, pp. 591–+.
- [19] Osterbrock, D. E. [1989], *Astrophysics of gaseous nebulae and active galactic nuclei*.
- [20] Rosenberg, D. L. [1995], A Numerical Study of Winds in Massive Binary Systems Containing Radio Pulsars, PhD thesis, THE UNIVERSITY OF NORTH CAROLINA AT CHAPEL HILL.
- [21] Stone, J. M. and Norman, M. L. [1993], ‘Numerical simulations of protostellar jets with nonequilibrium cooling. I - Method and two-dimensional results. II - Models of pulsed jets’, *ApJ* **413**, 198–220.
- [22] Toalá, J. A. and Arthur, S. J. [2011], ‘Radiation-hydrodynamic Models of the Evolving Circumstellar Medium around Massive Stars’, *ApJ* **737**, 100.
- [23] van Marle, A. J., Keppens, R. and Meliani, Z. [2011], ‘3-D simulations of shells around massive stars’, *Bulletin de la Societe Royale des Sciences de Liege* **80**, 310–315.
- [24] van Marle, A. J., Langer, N., Achterberg, A. and García-Segura, G. [2006], ‘Forming a constant density medium close to long gamma-ray bursts’, *A&A* **460**, 105–116.
- [25] van Marle, A. J., Langer, N. and García-Segura, G. [2005], ‘Constraints on gamma-ray burst and supernova progenitors through circumstellar absorption lines’, *A&A* **444**, 837–847.
- [26] Weaver, R., McCray, R., Castor, J., Shapiro, P. and Moore, R. [1977], ‘Interstellar bubbles. II - Structure and evolution’, *ApJ* **218**, 377–395.
- [27] Whalen, D. J. and Norman, M. L. [2008], ‘Three-Dimensional Dynamical Instabilities in Galactic Ionization Fronts’, *ApJ* **672**, 287–297.
- [28] Wrigge, M., Chu, Y.-H., Magnier, E. A. and Wendker, H. J. [2005], ‘X-Ray Emission from Wind-blown Bubbles. III. ASCA SIS Observations of NGC 6888’, *ApJ* **633**, 248–256.
- [29] Zhekov, S. A. and Park, S. [2011], ‘Suzaku Observations of the Prototype Wind-blown Bubble NGC 6888’, *ApJ* **728**, 135.